STASCAN deciphers fine-resolution cell-distribution maps in spatial transcriptomics by deep learning

Ying Wu[1,2], Jia-Yi Zhou[1,2,3], Bofei Yao[1,2], Guanshen Cui[1], Yong-Liang Zhao[1,2], Chun-Chun Gao[1], Shihua Zhang[4,5,6,9], Yun-Gui Yang[1,2,3,7,8,9]

Affiliations

[1]CAS Key Laboratory of Genomic and Precision Medicine, Beijing Institute of Genomics, Chinese Academy of Sciences and China National Center for Bioinformation, Beijing 100101, China

[2]University of Chinese Academy of Sciences, Beijing 100049, China

[3]College of Future Technology, University of Chinese Academy of Sciences, Beijing 100049, China

[4]NCMIS, CEMS, RCSDS, Academy of Mathematics and Systems Science, Chinese Academy of Sciences, Beijing 100190, China

[5]School of Mathematical Sciences, University of Chinese Academy of Sciences, Beijing 100049, China

[6]Key Laboratory of Systems Health Science of Zhejiang Province, School of Life Science, Hangzhou Institute for Advanced Study, University of Chinese Academy of Sciences, Hangzhou, 310024, China

[7]Sino-Danish College, University of Chinese Academy of Sciences, Beijing 101408, China

[8]Institute of Stem Cell and Regeneration, Chinese Academy of Sciences, Beijing 100101, China

[9]These authors jointly supervised this work: zsh@amss.ac.cn (S.Z.); ygyang@big.ac.cn (Y.G.Y.);

Abstract

The development of spatial transcriptomics (ST) technologies has enabled the deciphering of spatially cellular distribution by resolving gene expression profiles in tissue. However, the limited spatial resolution still poses new challenges in delineating fine-resolved cell maps. Here we propose a deep-learning approach STASCAN to simultaneously utilize gene expression and morphological information to improve the cellular resolution of captured domains and even gapped regions. Besides, STASCAN enables cell-type maps at subdivide-spot resolution and constructs the 3D spatial cell map from histology images alone. We applied STASCAN to spatial transcriptomics data of different species and tissues, and observed significantly improved cell granularity and detailed cell-distribution maps. In planarian, STASCAN depicted specific tissue structures composed of seven major cell types and contributed to reconstructing 3D digital vital models. STASCAN accurately pinpointed the boundary of distinct cell layers in human intestinal tissue, specifically identified a tiny smooth muscle bundle structure in human lung tissue and redrew spatial structural variation of cell-type niches in human cardiac tissue. In short, STASCAN displays obvious advantages in achieving precise cell annotation, revealing a finer organizational structure, and demonstrating the potential applications in studying cellular interactions in the tissue microenvironment.

Introduction

The spatial distribution and function of cells are intimately related, and their characterization will help to gain a deeper understanding of their function and potential impact on biological processes such as development and disease[1]. The emerging spatial transcriptomics (ST) technologies allow to capture of gene expression while preserving spatial context in tissue, which improves understanding of the structure and the cellular composition of different organs in different species[2-4].

Current ST technologies are typically divided into two categories: (1) imaging-based approaches, capturing genes corresponding to the targeted probes through *in situ* sequencing or *in situ* hybridization, which can achieve single-cell resolution but are limited by low throughput, biased coverage for pre-selected gene targets, and expensive specialized equipment; and (2) next-generation sequencing (NGS)-based approaches, capturing transcripts from tissue combined with encoded spatial positional information before next-generation sequencing[1,2]. By contrast, NGS-based approaches have been more widely applied owing to their advantages of higher throughput, unbiased coverage for transcriptome, and more accessible commercial products[5].

A vital limitation of NGS-based approaches is the spatial resolution restricted by the area and sparsity of captured domains[6]. For example, the captured domains (defined as spots) of Visium are 55 μm in diameter with a space of 100 μm, which are too large to capture the cells at single-cell resolution and too sparse to measure the cells in the gap regions[7]. Other approaches, such as Slide-seq[8], DBiT-seq[4], HDST[3], and Stereo-seq[9], choose much smaller or densely captured domains but are still perplexed by multiple cells or fractions within a single spot. In particular, the cells located in gap regions cannot be captured, leading to limited spatial resolution in both 2D and 3D levels. Current ST technologies enable us to depict cellular maps from a regional tissue section, and 3D cellular maps of organs can be constructed by being applied to consecutive tissue sections. However, its application is still hindered by the facts of costly experiments and sparsity between consecutive tissue sections rendering low resolution of the z-axis in 3D[5,10,11].

To improve the cellular resolution of ST technologies, current computational methods typically resolve gene profiles to perform cell-type deconvolution by integrating ST data with signatures of single-cell references and annotating cell types for captured domains[12], such as Cell2location[13], Seurat[14], and RCTD[15]. However, these methods only aim at inferring the proportion or abundance of cell type on captured domains and obtaining computationally improved cellular resolution within captured domains, whereas how to enhance spatial resolution by predicting cell distribution on gap regions between captured domains in a tissue section remains to be solved, and it is still infeasible to impute cell distribution between tissue sections to improve

cellular resolution in the z-axis.

Additionally, except for gene expression information in sequencing data, morphological information is also usually used to identify and character cell types of medical images[16-18]. Existing deconvolution methods tend to only focus on gene expression information while the morphological information carried by images in the ST dataset is mostly ignored, which may lead to not only the reduced accuracy of cell annotation due to the potential 'dropout' of marker genes[19,20], but also the lost support of image information to remedy for cellular resolution. There are some emerging computational methods combining gene expression information and morphological information in annotating cell types in ST data, such as Tangram[20] and MUSE[21]. However, apart from utilizing image information to improve the accuracy of cell annotation in captured domains, none of them enable improvement of spatial cellular resolution on 2D with gap regions or 3D with the z-axis.

Some developed methods leverage ST data and matched histology images to predict spatial resolved gene profiles and enable the prediction of gene expression information from images alone, greatly enhancing gene expression information at the spatial resolution[22-24]. However, combining sequencing data and image information to enhance cellular resolution in spatial transcriptomics is still lacking. Due to the limitation of cell-type deconvolution methods, the performance of these gene expression-imputing models needs to be improved further[23,24].

To this end, we propose a Spatial TrAnscriptomics-driven Spatially Cellular ANnotation tool STASCAN. STASCAN enables cell-type predictions on gap regions and super-resolved annotation of cells within capture regions, thereby enhancing spatial resolution with finer organizational structure. In addition, STASCAN succeeds in generating cell distribution maps from histological images of adjacent sections without sequencing, helping to construct a more detailed 3D cellular atlas of organs with lower ST experimental costs. Furthermore, we evaluated the applicability of STASCAN in different organizational spatial datasets and consistently found that STASCAN significantly improved cell granularity and displayed more comprehensively resolved cell distribution characteristics such as a tiny oval structure identified by STASCAN, which was confirmed as a smooth muscle bundle near the tracheal wall and has not been detected by other annotation tools. Moreover, STASCAN provided a finer distribution of cell-type niches in cardiac tissue, facilitating understanding of cardiac remodeling after myocardial infarction.

Results

Overview of STASCAN

STASCAN adopts a deep learning model to utilize both the spatial gene expression profiles from the ST technology (10x Visium) and the

corresponding histological images, to depict a fine-resolution cell distribution map in tissues (**Fig. 1a**). Firstly, STASCAN extracts the spot images from slide images based on location information, and infers highly reliable cell labels for each spot based on spatial gene expression using deconvolution during the pre-labeling process. Secondly, STASCAN constructs a base convolutional neural network (CNN) model and trains the base CNN model using the cell-type labeled spot images as input. Additionally, STASCAN provides optional section-specific training, which can fine-tune the base CNN model through transfer learning to improve the prediction accuracy for a specific single section. Finally, through ample training, STASCAN can accurately predict cell types solely based on histological images (**Fig.1a**, **Supplementary Fig.1** and **Methods**).

STASCAN is further designed into three application modules: (1) cell annotation for the embedded unseen spots, which is based on image features of the measured raw spots, assigning predicted cell type for each unseen spot, and merging the unseen and raw spots to achieve a super-resolved cell distribution (**Fig. 1b**); (2) cell annotation for subdivided spots, which learns features from the sub-spot images with optional pseudo-labels to obtain a sub-resolution cell distribution (**Fig. 1c**); (3) cell annotation for unseen sections, which learns the spot images from measured ST sections with optional pseudo-labels to predict the cell distribution on adjacent unmeasured tissue sections from the consecutive sections for constructing 3D cell atlas (**Fig. 1d**).

STASCAN achieves more precise cell annotation

To quantitatively evaluate the spatial cell annotation performance of STASCAN, we first applied it to resolve the planarian ST dataset, which includes ten measured ST sections (containing both spatial gene expression data and histological images) and nine unmeasured sections adjacent to ST sections (only containing histological images)[25]. Given the comprehensiveness of the planarian dataset, we first constructed a base model using 1,829 spot images extracted from 10 collected sections to learn the features of seven main cell types, including epidermal, gut, muscle, neoblast, neuronal, parenchymal, and secretory cells (**Supplementary Fig. 2a, b**, **Supplementary Table 1** and **Methods**). Although there was confusion in predicting neoblast and parenchymal cells due to the limited training samples, most cell types were annotated with a recall rate of over 78% (**Fig. 2a** and **Supplementary Fig. 2c**). In addition, the learned model showed excellent accuracy in predicting cell types, with the area under the curve (AUC) calculated from the receiver operating characteristic (ROC) curves reaching as high as 0.936 to 0.996 (**Fig. 2b**). Besides, considering the potential batch effect among different ST sections, we performed section-specific training based on the base model (**Methods**). The results from the section-specific model showed a significant improvement in accuracy with higher AUC values compared with the base model, indicating that section-specific training is beneficial for the improved

prediction performance of the whole frame (**Fig. 2c**).

To evaluate the performance of STASCAN in predicting dominant cell types on raw spots, we compared it with Cell2location[13], Seurat[14], and RCTD[15]. We observed that Cell2location could characterize most cell distribution but with a low sensitivity for epidermal cells, Seurat also showed strong annotation bias for epidermal cells, leading to mislabeling for other cell types, and RCTD displayed some positive annotation but lost annotation information for most neuronal and secretory cells. Thus, only gene expression-based cell-type deconvolution will result in varied degrees of biases for cell annotation (**Fig. 2d**). In contrast, STASCAN displayed more precise predictive performance in cell annotation, and accurately pinpointed the spatial distribution of seven main types of cells, confirmed by their known biological functions[26] (**Fig. 2d**, **Supplementary Fig. 2d,e**). For example, corresponding to clear tissue structures shown by hematoxylin and eosin (H&E) staining, the epidermal cells draw the contour of the planarian body, gut cells draw the location of the intestine, and muscle along with neuronal cells draw the anatomy of the pharynx (**Fig. 2d** and **Supplementary Fig. 2d**). To further evaluate the predictive performance of different methods, we manually annotated the cell types of each raw spot based on the morphologic features (**Fig. 2d**). As expected, the cell distribution predicted by STASCAN is highly correlated with that of manual annotations, significantly superior to other methods (**Fig. 2e**). In short, STASCAN could precisely infer spatial cell distribution map through integrating spatial gene expression data and morphology information to predicted cell types.

STASCAN achieves super-resolution cellular patterns and improved 3D reconstruction in planarian

Next, we assessed the capabilities of STASCAN in different predicting modules using the planarian dataset[25]. When using Seurat and Cell2location to predict the spot cell types for pre-labeling, approximately half of the raw spots cannot be assigned with reliable cell labels (**Supplementary Fig. 2a** and **Methods**). This issue may be due to the noises generated by the complex signatures of gene expression in each spot, indicating the drawback of deconvolution in determining cell types (**Fig. 3a**). Choosing the other half of raw spots with credible labels as the prior spots to train the model, STASCAN achieved the reliable ability of cell type annotation based on images and depicted super-resolved cell distribution map (**Fig. 3a**). Firstly, STASCAN performed cell annotation for the unseen spots and demonstrated an enhanced resolution of cell distribution through combining both unseen spots and raw spots. The enhanced cell distribution map was highly consistent with H&E staining images, highlighting the relevant structures that were not shown at the raw resolution, such as the ventral nerve cord, genital chamber, pharynx, and contour (**Fig. 3a** and **Supplementary Fig. 2d**). Besides, it was highly consistent with the distribution of corresponding cell markers reported in

previous literature[26] (**Fig. 3b** and **Supplementary Fig. 3a**).

Furthermore, STASCAN pinpointed the composition of cell mixtures and their distinct locations at sub-resolution, effectively distinguishing cell types of each subdivided spot, and displaying a more detailed distribution of fine-grained cells (**Fig. 3c**). For example, STASCAN sensitively allocated secretory and neoblast cells around the contour into sub-divided positions according to the morphological differences. STASCAN also identified muscle cells located at the junction of the pharynx and intestine at sub-resolution and were consistent with the biological priori information (**Fig. 3c**), which were not discovered at raw resolution from a group of gut cells. In addition, we utilized STASCAN to predict the enhanced sub-resolved distribution of gut cells, obtaining the fine-grained distribution of gut cells and reproducing the classical branching structure of the planarian intestinal tract (**Fig. 3d**). These results indicate that STASCAN significantly enhances cell granularity at sub-resolution, facilitating depiction of instrumental sub-structure with fine-grained cells.

Last but not least, STASCAN achieved the prediction of cell distribution in the unseen sections only by learning the adjacent ST sections of H&E images (**Fig. 3e** and **Supplementary Fig. 3b**). In line with the biological interpretation that the cell distribution between two consecutive sections should be similar, the structure similarity index measure (SSIM) (ranging from 0.67 to 0.89) was linearly correlated with the spacing distance between adjacent images and ST sections, demonstrating the prediction accuracy of cell annotation for unseen sections (**Fig. 3f**, **Supplementary Fig. 3b** and **Methods**). Furthermore, we generated raw and unseen spots from ST sections and adjacent images, applied STASCAN to predict cell types for those spots, and then reconstructed 3D models for different structures with cellular patterns (**Fig. 3g**). The model displayed the cell distribution in three-dimensional, with improved cellular resolution in spatial and promoted utilization of staining images without ST sequencing.

STASCAN recognizes well-defined boundaries of distinct cell layers in the human intestinal tissue

To further evaluate the performance of STASCAN for ST datasets on different tissue architectures, we introduced the ST datasets of eight slides generated from diverse sampling locations and time points of human intestinal tissue[27]. We applied STASCAN to train on each slide with different sizes of prior spots, ranging from 297 to 1,551 and observed stable performances. (**Supplementary Fig. 4a-c**, **Supplementary Table 1** and **Methods**).

Next, we applied STASCAN to predict cell types of unseen spots. Compared with the cell distribution of prior spots annotated by other methods, STASCAN stratified cell populations to finer regional layers. For example, in comparison with other methods only roughly distinguishing the distribution of different cells in certain spatial areas, STASCAN was able to delineate the borders of cell layers among the intestinal epithelium, fibroblasts, and

muscularis, greatly enhancing the cellular spatial patterns (**Fig. 4a** and **Supplementary Fig. 5**).

Then, we applied STASCAN to draw the spatial distribution map of fine subtypes in the human intestinal tissue (**Fig. 4b**). Actually, we labeled three anatomical layers of the intestinal tissue related to the morphological structures of H&E staining, including muscularis, fibroblasts and epithelium layers, listed based on their distance from the intestinal edge (**Fig. 4c**). When evaluating four epithelium subtypes occupying an absolute proportion of the epithelium layer, we found that compared to the results of alternative method at raw-resolution, STASCAN not only highlights the precise distribution of these subtypes but also accurately locates the positions of distinct subtype cells (**Fig. 4b, d, e** and **Supplementary Fig. 6a**). For instance, distal epithelium subtype cells tend to gather closer to the boundary of the epithelium layer and the fibroblast layer, and proximal epithelium subtype cells are prone to assemble to the surface of the epithelium layer at sub-resolution. Besides, distal stem cells were correctly predicted to be located in the epithelium layer at sub-resolution, however, at raw-resolution, a part of distal stem cells were abnormally predicted to be located in the fibroblasts layer (**Fig. 4d, e** and **Supplementary Fig. 6b**).

In addition, we performed STASCAN on a pair of identical and adjacent sections of the intestinal tissue (**Methods**), and the high correlation between them further confirmed the accuracy and reliability of the prediction (**Supplementary Fig. 7a, b**).

STASCAN reveals novel structure at enhanced resolution in the human lung tissue

We expect STASCAN to discover novel organizational structures ignored at raw spatial resolution. We applied STASCAN on a human lung dataset[28] sampled from the proximal airway. We previously redefined 13 reference cell types that could better showcase the organizational structure and annotated 822 ST spots with seven dominant cell types to train the STASCAN (**Supplementary Fig. 8a-e**, **Supplementary Table 1** and **Methods**). With enhanced resolution, STASCAN showed more precision cellular and structural patterns of human lung tissue. Besides, we noticed that STASCAN sensitively identified a tiny oval-shaped structure that was highly consistent with the H&E staining images, which was confirmed as the smooth muscle bundles neighboring the tracheal wall. However, this structure was not demonstrated at raw resolution by prior spots, convincingly proving the capability of STASCAN to reveal refined structures of spatial regions (**Fig. 5a** and **Supplementary Fig. 8c**).

Furthermore, we compared the ability of STASCAN with other methods in revealing tissue structures with cellular patterns. The results showed that STASCAN could clearly depict the silhouette of the airway with basal and neuroendocrine cells and the cricoid cartilage structure surrounded by goblet

cells, mucous cells, smooth muscle cells, pericytes, etc. Moreover, the smooth muscle tissue traced by smooth muscle cells and pericytes in the left bottom of the slide was only identified by STASCAN (**Fig. 5b** and **Supplementary Fig. 8c**). Briefly, compared with the cell distribution pattern identified by other methods, STASCAN displayed absolute advantages in identifying and characterizing spatial specific structures, which better reflects the anatomical structure after imputation.

STASCAN redraw pathological spatial structural variation of human cardiac tissue after myocardial infarction

To further demonstrate the applicability of STASCAN, we adopted it to reanalyze the human cardiac datasets[29], which included 17 slides from normal hearts and pathological ones after myocardial infarction (**Supplementary Figs. 9a,b, 10**, **Supplementary Table 1** and **Methods**). We first grouped these slides according to their sampling regions[29], including normal non-transplanted donor hearts as controls, necrotic (ischaemic zone and border zone), and unaffected regions (remote zone), and regions at later stages after myocardial infarction (fibrotic zone). After performing STASCAN to enhance the spatial cell distribution, we focused on two slides with missing spots that were filtered out due to scanty genes and unique molecular identifiers (UMI) measured in the original literature[29] (**Fig.6a** and **Supplementary Figs. 11-15a**). In these two slides, STASCAN not only more accurately depicted the cell distribution pattern of tissue structures, but also predicted the potential cell distributions in the missing areas. Especially for the serious missing in the slide_ACH0010 sampled from the ischaemic zone, STASCAN better imputed the reasonable diffusion of the cardiomyocyte, fibroblast, and myeloid cells in line with the histological morphology (**Fig. 6a**). The proximity of the latter two cells indicated a strong dependence with each other on the areas of immune cell infiltration and scar formation[29].

Furthermore, we performed unsupervised clustering for spots based on the composition of cell annotations predicted by STASCAN and mapped the clusters defined as cell-type niches to the spatial regions (**Fig. 6b, c, f** and **Supplementary Figs. 11-15b**). Through redrawing spatial distributions for these cell-type niches, the cardiac tissue manifested more delicate spatial patterns compared with the spatial distributions of dominant cell annotation, which were consistent with histological morphology and detailed structural variation during physiological and pathological processes.

Besides, these niches identified based on diverse cell propositions revealed more elaborate cell interacting microenvironments with potential biological insights (**Fig. 6d, e** and **Supplementary Figs. 11-15c**). For example, we observed myogenic cell-type niches (0, 1, and 2) mainly displaying characteristics of cardiomyocyte cells, and fibrotic cell-type niches (3, 4, 5, 6, and 7) mainly presenting characteristics of fibroblast cells, in the slide_ACH006 sampled from the fibrotic zones. On the aspect of spatial

distributions, the myogenic cell-type niches could jointly characterize the myocardial structure, and the fibrotic cell-type niches distinguished by fibroblast cell proposition indicated different fibrosis processes during the lesion. Especially, there was a measure of characteristics of vSMCs and endothelial cells in niches 3 and 4 for depicting the spatial structure of the cardiac vasculature. In addition, in slide_ACH0010, we observed inflammatory cell-type niches (4, 5, 6, and 7) which mainly exhibit characteristics of myeloid and mast cells, apart from myogenic cell-type niches (0 and 1) and fibrotic cell-type niches (2 and 3). These three types of niches took up distinct spatial regions, but there was niche 7 located at the intersection, in line with the proposition of cardiomyocyte, fibroblast, myeloid, and mast cells in the niche 7. Especially, niches 2, 3, 4, and 5 showed co-enrichment between myeloid and fibroblast cells, in accordance with the role of macrophages in fibroblast activation[30] and fibroblast cells in macrophage attraction[31]. Overall, STASCAN expands the application of niche distribution and provides better insights into understanding cellular microenvironment interactions.

Discussion

Although remarkable progress has been achieved in deciphering the distribution and interaction of cells in tissues by current spatial transcriptomics, the disadvantages in spatial resolution limit its application. The development of computational algorithms is crucial for spatial transcriptomic data analysis. Here, we develop STASCAN to depict enhanced spatially resolved cell atlases by leveraging histological images and spatial gene expression for comprehensive cell annotation.

Compared with the traditional image-based CNN model, STASCAN integrates gene expression and image information, and gene expression helps automatically label spots used for training without manual annotation. Meanwhile, images extend a new perspective and supplement the information that sequencing can’t provide. Additionally, STASCAN can accurately extract features and improve the accuracy of the model through transfer learning and pseudo-labeling. Thus, STASCAN can effectively resolve images and use the image information as the main reference for cell type determination, which helps to predict cell distribution and further construct fine-resolved 3D spatial cell distribution maps. The application on ST dataset generated by Visium is most popular because of commercial platforms and accessible equipment[5]. The technical framework of STASCAN can be further designed for other sequencing-based spatial transcriptomics dataset.

Through full use of sequencing and image data, STASCAN not only annotates accurately the cell types on raw ST spots but also enables the prediction of cell distribution in the ST captured gaps. Besides, STASCAN fully utilizes the image information of continuous sections to construct 3D tissue

models without expensive ST experimental costs, laying the foundations for expanding the future frontier in 3D cellular atlas. We performed STASCAN in different species and tissues and observed a substantial advance over current methods in spatial cell annotation. In planarian, STASCAN could successfully prospect cell distribution of unmeasured regions and distinct tissue structures that couldn't be observed at the raw resolution but were critical in constructing stereoscopic cell distribution in 3D space. In addition, STASCAN can discover precise tissue structures with enhanced cell annotation. In human lung tissue, only at enhanced spatial resolution, STASCAN identified a specific structure that was made up of a group of smooth muscle cells located near the tracheal wall and related to the regulation of intra-pulmonary airway caliber[32].

The low resolution of sequencing-based spatial transcriptomics is mainly attributed to the spacing of capture spots, which are not small enough to achieve single-cell resolution[6]. Most current methods estimate the proportion or abundance of each cell type from the cell mixtures on the capture spots but are incapable of assigning each cell into exact locations within each spot. Although Tangram provides a computer vision module that segments cell nuclei based on histological images and predicts single cell type in each spot, it performs random cell assignment within a spot for the specifically segmented cells and still cannot resolve cell position within spots[20]. In comparison, STASCAN proposes a predicting module at sub-resolution, allowing assigning cell types for sub-divided spots depending on the tissue morphological features corresponding to the position.

The advantages of STASCAN permit its wider range of applications. For example, STASCAN can be effectively used to predict cell distribution of some regions with missed sequencing data due to the low number of captured UMIs and genes. In human cardiac tissues, STASCAN could fill in the missing data, and help to display an extensive spatial proximity distribution of fibroblast and myeloid cells in the vicinity of scar tissue, which facilitates a better understanding of the relationship between fibroblasts and immune cells in myocardial infarction, such as immune factors in stimulating fibroblast transformation[33]. Additionally, the annotation of cell proposition generated by STASCAN is supported to cluster different cell-type niches, providing novel insights into the microenvironment at cellular resolution. Also in human cardiac tissues, STASCAN could generate distinct niches including inflammatory, myogenic, and fibrotic cell-type niches, with the best presentation of the dynamic diversity of cells in the microenvironment during myocardial infarction.

In summary, STASCAN is a universal and precise cell type prediction method, which integrates image and expression information to predict complex spatial distributions in tissues. Through the applications of this approach in planarian and different human tissues, STASCAN has demonstrated superior performance in enhancing spatial resolution and discovering novel structures, which has potential perspectives in resolving cell type distribution in various types of tissues related to different stages of development, regeneration, and

disease. The positional relationships of different cell types determined by STASCAN provided new insights into cell crosstalk critical in orchestrating organismal development and homeostasis. Besides, STASCAN fully utilizes more easily acquired image datasets under various biological conditions, which through extensive data training, is likely used to infer subtypes of pathological cells and further link spatial cellular distribution to disease diagnosis cost-efficiently without the need for sequencing.

Reference

1 Longo, S. K., Guo, M. G., Ji, A. L. & Khavari, P. A. Integrating single-cell and spatial transcriptomics to elucidate intercellular tissue dynamics. *Nat Rev Genet* **22**, 627-644 (2021).

2 Rao, A., Barkley, D., Franca, G. S. & Yanai, I. Exploring tissue architecture using spatial transcriptomics. *Nature* **596**, 211-220 (2021).

3 Vickovic, S. *et al.* High-definition spatial transcriptomics for in situ tissue profiling. *Nat Methods* **16**, 987-990 (2019).

4 Liu, Y. *et al.* High-spatial-resolution multi-omics sequencing via deterministic barcoding in tissue. *Cell* **183**, 1665-1681 e1618 (2020).

5 Moses, L. & Pachter, L. Museum of spatial transcriptomics. *Nat Methods* **19**, 534-546 (2022).

6 Stark, R., Grzelak, M. & Hadfield, J. RNA sequencing: the teenage years. *Nat Rev Genet* **20**, 631-656 (2019).

7 Ståhl, P. Visualization and analysis of gene expression in tissue sections by spatial transcriptomics. *Science* **353**, 78-82 (2016).

8 Stickels, R. R. *et al.* Highly sensitive spatial transcriptomics at near-cellular resolution with Slide-seqV2. *Nat biotechnol* **39**, 313-319 (2021).

9 Chen, A. *et al.* Spatiotemporal transcriptomic atlas of mouse organogenesis using DNA nanoball-patterned arrays. *Cell* **185**, 1777-1792. e1721 (2022).

10 Asp, M. *et al.* A spatiotemporal organ-wide gene expression and cell atlas of the developing human heart. *Cell* **179**, 1647-1660 e1619 (2019).

11 Chen, A. *et al.* Single-cell spatial transcriptome reveals cell-type organization in the macaque cortex. *Cell* **186**, 3726-3743.e24 (2023).

12 Li, B. *et al.* Benchmarking spatial and single-cell transcriptomics integration methods for transcript distribution prediction and cell type deconvolution. *Nat Methods* **19**, 662-670 (2022).

13 Kleshchevnikov, V. *et al.* Cell2location maps fine-grained cell types in spatial transcriptomics. *Nat Biotechnol* **40**, 661-671 (2022).

14 Stuart, T. *et al.* Comprehensive integration of single-cell data. *Cell* **177**, 1888-1902 e1821 (2019).

15 Cable, D. M. *et al.* Robust decomposition of cell type mixtures in spatial transcriptomics. *Nat Biotechnol* **40**, 517-526 (2022).

16 Perlman, Z. E. *et al.* Multidimensional drug profiling by automated microscopy. *Science* **306**, 1194-1198 (2004).

17 Feldman, D. *et al.* Optical pooled screens in human cells. *Cell* **179**, 787-799 e717 (2019).

18 Loo, L. H., Wu, L. F. & Altschuler, S. J. Image-based multivariate profiling of drug responses from single cells. *Nat Methods* **4**, 445-453 (2007).

19 Maaskola, J. *et al.* Charting tissue expression anatomy by spatial

transcriptome deconvolution. Preprint at *bioRxiv* https://doi.org/10.1101/362624 (2018).

20 Biancalani, T. *et al.* Deep learning and alignment of spatially resolved single-cell transcriptomes with Tangram. *Nat Methods* **18**, 1352-1362 (2021).

21 Bao, F. *et al.* Integrative spatial analysis of cell morphologies and transcriptional states with MUSE. *Nat Biotechnol* **40**, 1200-1209 (2022).

22 He, B. *et al.* Integrating spatial gene expression and breast tumour morphology via deep learning. *Nat Biomed Eng* **4**, 827-834 (2020).

23 Bergenstråhle, L. *et al.* Super-resolved spatial transcriptomics by deep data fusion. *Nat Biotechnol* **40**, 476-479 (2021).

24 Monjo, T., Koido, M., Nagasawa, S., Suzuki, Y. & Kamatani, Y. Efficient prediction of a spatial transcriptomics profile better characterizes breast cancer tissue sections without costly experimentation. *Sci Rep* **12**, 4133 (2022).

25 Cui, G. *et al.* Spatiotemporal transcriptomic atlas reveals the dynamic characteristics and key regulators of planarian regeneration. *Nat Commun* **14**, 3205 (2023).

26 Benham-Pyle, B. W. *et al.* Identification of rare, transient post-mitotic cell states that are induced by injury and required for whole-body regeneration in Schmidtea mediterranea. *Nat Cell Biol* **23**, 939-952 (2021).

27 Fawkner-Corbett, D. *et al.* Spatiotemporal analysis of human intestinal development at single-cell resolution. *Cell* **184**, 810-826 e823 (2021).

28 Kadur Lakshminarasimha Murthy, P. *et al.* Human distal lung maps and lineage hierarchies reveal a bipotent progenitor. *Nature* **604**, 111-119 (2022).

29 Kuppe, C. *et al.* Spatial multi-omic map of human myocardial infarction. *Nature* **608**, 766-777 (2020).

30 Shook, B. A. *et al.* Myofibroblast proliferation and heterogeneity are supported by macrophages during skin repair. *Science* **362**, eaar2971 (2018).

31 Pakshir, P. *et al.* Dynamic fibroblast contractions attract remote macrophages in fibrillar collagen matrix. *Nat Commun* **10**, 1850 (2019).

32 An, S. *et al.* Airway smooth muscle dynamics: a common pathway of airway obstruction in asthma. *Eur Respir J* **29**, 834-860 (2007).

33 Cho, N., Razipour, S. E. & McCain, M. L. Featured Article: TGF-β1 dominates extracellular matrix rigidity for inducing differentiation of human cardiac fibroblasts to myofibroblasts. *Exp Biol Med* **243**, 601-612 (2018).

34 Abadi, M. *et al*. TensorFlow: Large-Scale Machine Learning on Heterogeneous Distributed Systems. *ArXiv*, abs/1603.04467 (2016).

35 Simonyan, K. Z., A. Very deep convolutional networks for large-scale image recognition. *CoRR*, abs/1409.1556 (2014).

Figure legends

Fig. 1. Overview of STASCAN.

(a) Architecture of the STASCAN framework. STASCAN infers fine-resolution cell distribution with spatial transcriptomic (ST) data based on a deep learning model. Preprocessed spot images and dominant cell labels from slide images and gene expression data are taken as input to train a base CNN model. STASCAN provides an optional process to conduct section-specific training, which performs transfer learning to learn the characteristics of specific sections.

(b) Architecture of cell annotation for unseen spots. STASCAN infers cell types for unseen spot images to decipher the super-resolution cell distribution of a ST slide. Unseen spots, the artificial spots among the unmeasured area.

(c) Architecture of cell annotation for subdivided spots. STASCAN infers cell types of subdivided spot images to decipher the sub-resolution cell distribution of a ST slide. Raw spots, spots at raw resolution. Subdivided spots, spots by dividing raw spots for high resolution.

(d) Architecture of cell annotation for unseen sections. STASCAN predicts cell types of simulated spots on adjacent images by learning characteristics of prior spot images from ST sections, depicting 3D cell distribution of tissue. Sections, ST sections with sequencing data. Adjacent images, adjacent H&E images without sequencing data.

Fig. 2. STASCAN shows better performance for cell-type prediction.

(a) Heatmap showing the confusion matrix of the prediction and truth value of the base model for the 5-fold cross-validation in the planarian dataset. The number in each box represents the recall value.

(b) ROC curves of each major cell type of the base model in the planarian dataset. The number in each pair of parentheses represents the AUC value.

(c) Violin plot showing the AUC values of the base model (n = 7) and specific model (n = 70), respectively. P value is calculated using two-sided Wilcoxon signed-rank tests.

(d) Cellular distribution of section 23 in the planarian dataset. Left, H&E staining image showing general morphology. Right, spatial plots (x and y axis) depicting the distribution of the major cell types annotated by STASCAN, Cell2location, Seurat, RCTD, and manual annotation.

(e) Boxplot showing the Pearson correlation between cell distribution of section 23 that annotated by manual and alternative methods, respectively (n = 683, 683, 683, 681). P values are calculated using two-sided Wilcoxon signed-rank tests.

Fig. 3. STASCAN provides comprehensive and multidimensional cell annotation in the planarian.

(a) Tissue regions of the planarian in section 6. Left top, H&E staining image showing general morphology. Left center, spatial plot (x and y axis) covering the H&E staining image depicting distribution for the major cell types on the prior spots. Prior spots, the spots that are predicted to be the same cell types by both the Cell2location and Seurat at the raw resolution. Left bottom, spatial plot (x and y axis) covering the H&E staining image depicting distribution for the major cell types on the fully-tiled spots. Fully-tiled spots, containing both the raw spots and unseen spots. Raw spots, containing prior spots and other spots at the raw resolution. The latter were assigned with cell types by STASCAN. Unseen spots, the artificial spots among unmeasured areas, inferred with cell types by STASCAN. Right, enlarged view of the black framed area, arranged by left, middle, and right frame.

(b) Visualizations of cell distribution for three major cell types and expression patterns of corresponding marker genes. Top, cell distribution annotated by STASCAN. Bottom, whole-mount in situ hybridization of classic gene markers (from published research[26]).

(c) Tissue regions of the planarian in section 25. Left top, H&E staining image showing general morphology. Left center, spatial plot (x and y axis) covering H&E staining image depicting cell distribution for the major types annotated by STASCAN at raw resolution. Left bottom, spatial plot (x and y axis) covering the H&E staining image to decipher cell distribution for the major types annotated by STASCAN at sub-resolution. Right, enlarged view of the black framed area, arranged by left and right frame.

(d) Spatial plots (*x* and *y* axis) depicting cell distribution for gut cells. Left, cell distribution predicted by STASCAN at raw resolution. Middle, cell distribution predicted by STASCAN at sub-resolution. Right, cell distribution predicted by STASCAN at sub-enhanced resolution.

(e) Tissue region of planarian in section 21 and adjacent image 22. Left, H&E staining image and spatial plots (*x* and *y* axis) depicting cell distribution predicted by STASCAN of section 21. Right, H&E staining image and spatial plots (*x* and *y* axis) to decipher cell distribution predicted by STASCAN of adjacent image 22.

(f) Heatmap showing the values of SSIM between the cell distribution of adjacent images and nether ST sections. Numbers on the coordinate axis represent the order of ST sections and adjacent images from the same consecutive sections set.

(g) 3D spatial plots (x, y, and z axis) depicting 3D distribution of two selected cell types. Top, muscle cell. Bottom, neoblast cell. Both 3D models are reconstructed with aligned outlines and spots from the ST section and adjacent images.

Fig. 4. STASCAN depicts spatial layers of distinct cell types in the human intestinal tissue.

(a) Tissue regions of the human intestinal tissue for both the 12 PCW colon (slide 3) and 19 PCW colon (slide 4) respectively. Left, H&E staining image showing general morphology. Middle, spatial plot (x and y axis) depicting distribution for the major cell types of the prior spots. Right, spatial plot (x and y axis) depicting super-resolution cell distribution for the major cell types of the fully-tiled spots. Slide numbers are shown in columns.

(b) Tissue regions of the human intestinal tissue for 19 PCW colon. Left, spatial plot (x and y axis) depicting cell distribution for epithelium subtypes inferred by Cell2location at raw resolution. Right, spatial plot (x and y axis) depicting cell distribution for epithelium subtypes inferred by STASCAN at sub-resolution.

(c) Schematic of muscularis, fibroblasts, and epithelium layers, colored in gradients according to the distance from the spot to the tissue edge.

(d) Spatial plots (*x* and *y* axis) depicting cell distribution for distal mature enterocytes. Left, cell distribution predicted by Cell2location at raw resolution. Right, cell distribution inferred by STASCAN at sub-resolution. The black lines represent the schematic of different morphological layers.

(e) Spatial plots (*x* and *y* axis) depicting cell distribution for distal stem cells. Left, cell distribution inferred by Cell2location at raw resolution. Right, cell distribution inferred by STASCAN at sub-resolution. The black lines represent the schematic of different morphological layers.

Fig. 5. STASCAN demonstrates the special structure of the human lung tissue.

(a) Tissue regions of the human proximal lung. Left, H&E staining image showing general morphology. Middle, spatial plot (*x* and *y* axis) depicting cell distribution for the major types on prior spots. Right, spatial plot (x and y axis) depicting super-resolution cell distribution for the major types on the fully-tiled spots.

(b) Spatial plots (*x* and *y* axis) depicting cell distribution for the three major types. Cell types are shown in columns, and alternative methods (STASCAN, Cell2locaiton, Seurat, and RCTD) used to annotate the corresponding cell type are shown in rows.

Fig. 6. STASCAN reveals the cell-type niches in human cardiac tissue after myocardial infarction.

(a) Tissue regions of the human cardiac tissue from the fibrotic zone (Slide_ACH006) and ischaemic zone (Slide_ACH0010) after myocardial infarction. Left, H&E staining image showing general morphology. Middle, spatial plot (*x* and *y* axis) depicting cell distribution for the major cell types on prior spots. Right, spatial plot (x and y axis) depicting super-resolution cell distribution for the major cell types on the fully-tiled spots. Slide numbers are shown in columns. Missing spots, spots removed from raw spots in the original literature due to the small number of measured genes and UMIs. FZ, fibrotic zone. IZ, ischaemic zone.

(b) Spatial plots (*x* and *y* axis) depicting spatial distribution for cell-type niches in slide_ACH006, which are assigned by unsupervised clustering of spots with the cell-type compositions.

(c) Spatial plots (*x* and *y* axis) depicting spatial distribution for cell-type niches in slide_ACH0010, which are assigned by unsupervised clustering of spots with the cell-type compositions.

(d) Bar plot showing the cell proposition of cell-type niches in slide_ACH006.

(e) Bar plot showing the cell proposition of cell-type niches in slide_ACH0010.

(f) Schematic of cell-type niches.

Figure 1

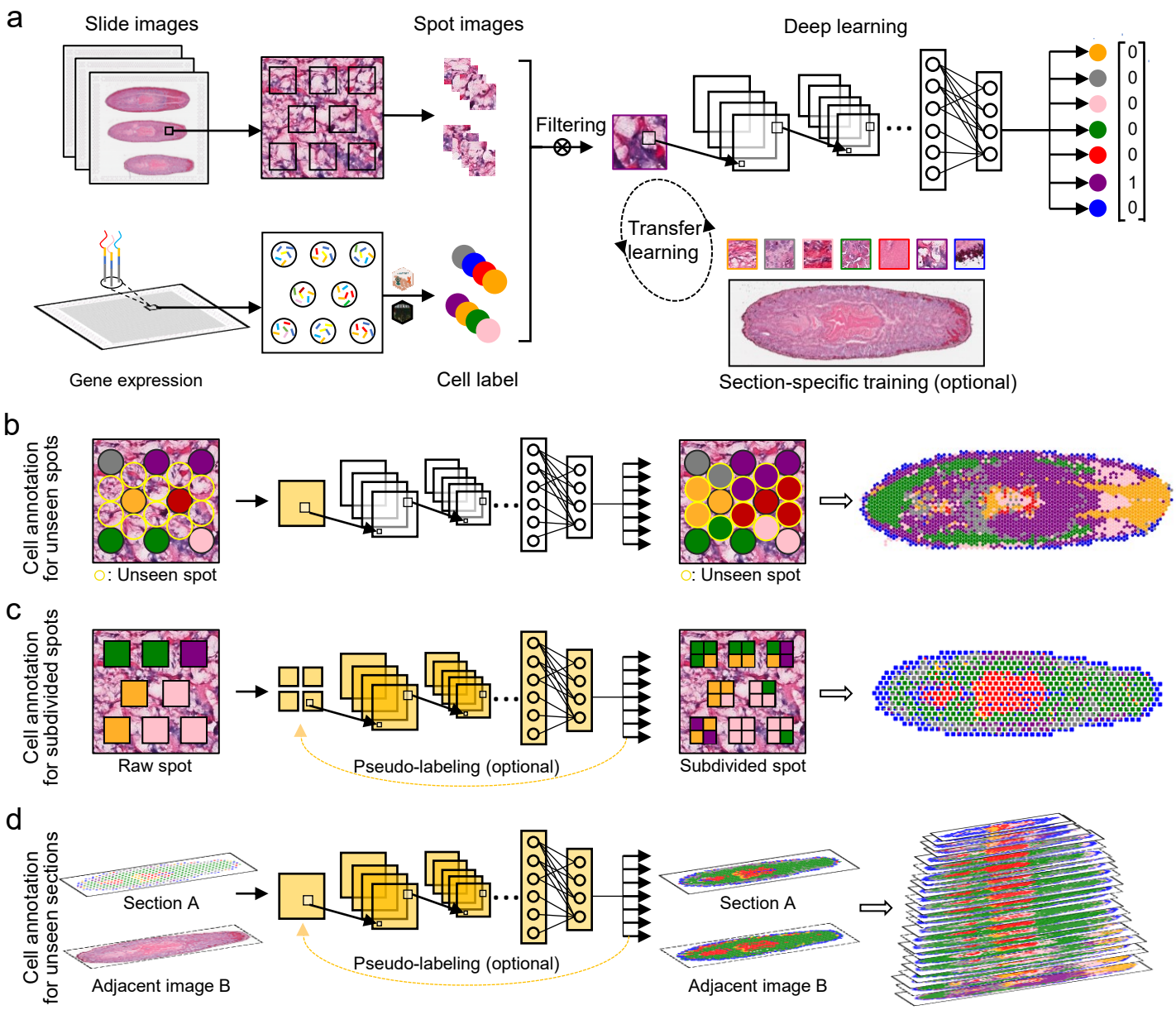
a
Slide images
Spot images
Deep learning
Filtering
Transfer learning
Gene expression
Cell label
Section-specific training (optional)
b
Cell annotation for unseen spots
: Unseen spot
: Unseen spot
c
Cell annotation for subdivided spots
Raw spot
Pseudo-labeling (optional)
Subdivided spot
d
Cell annotation for unseen sections
Section A
Adjacent image B
Pseudo-labeling (optional)
Section A
Adjacent image B

Figure 2

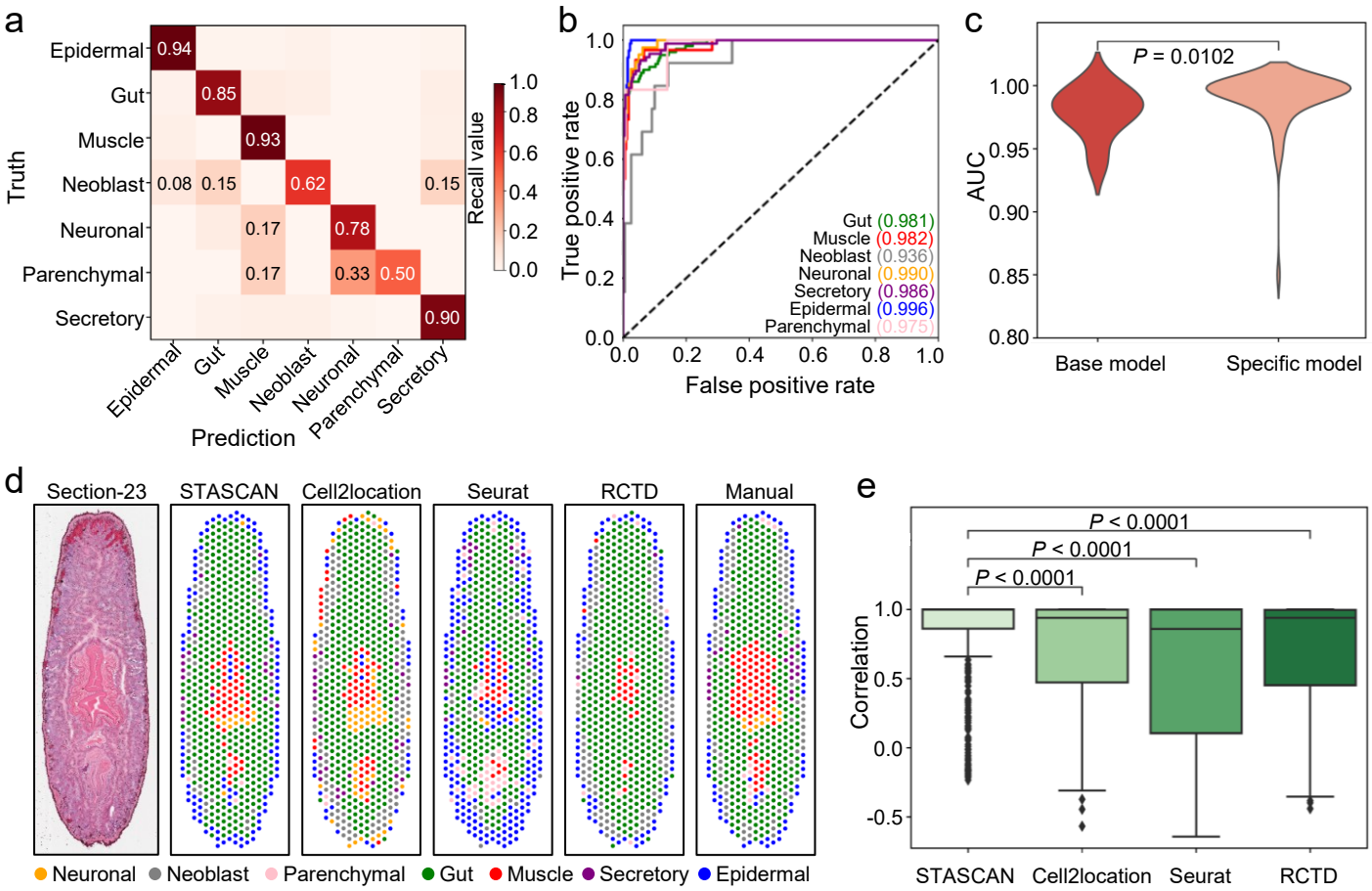
a
Epidermal
Gut
Muscle
Neoblast
Neuronal
Parenchymal
Secretory
Truth
Prediction
0.94
0.85
0.93
0.08 0.15 0.62 0.15
0.17 0.78
0.17 0.33 0.50
0.90
Recall value
1.0
0.8
0.6
0.4
0.2
0.0
b
True positive rate
False positive rate
Gut (0.981)
Muscle (0.982)
Neoblast (0.936)
Neuronal (0.990)
Secretory (0.986)
Epidermal (0.996)
Parenchymal (0.975)
c
AUC
P = 0.0102
Base model
Specific model
d
Section-23
STASCAN
Cell2location
Seurat
RCTD
Manual
Neuronal
Neoblast
Parenchymal
Gut
Muscle
Secretory
Epidermal
e
Correlation
P < 0.0001
P < 0.0001
P < 0.0001
STASCAN
Cell2location
Seurat
RCTD

Figure 3

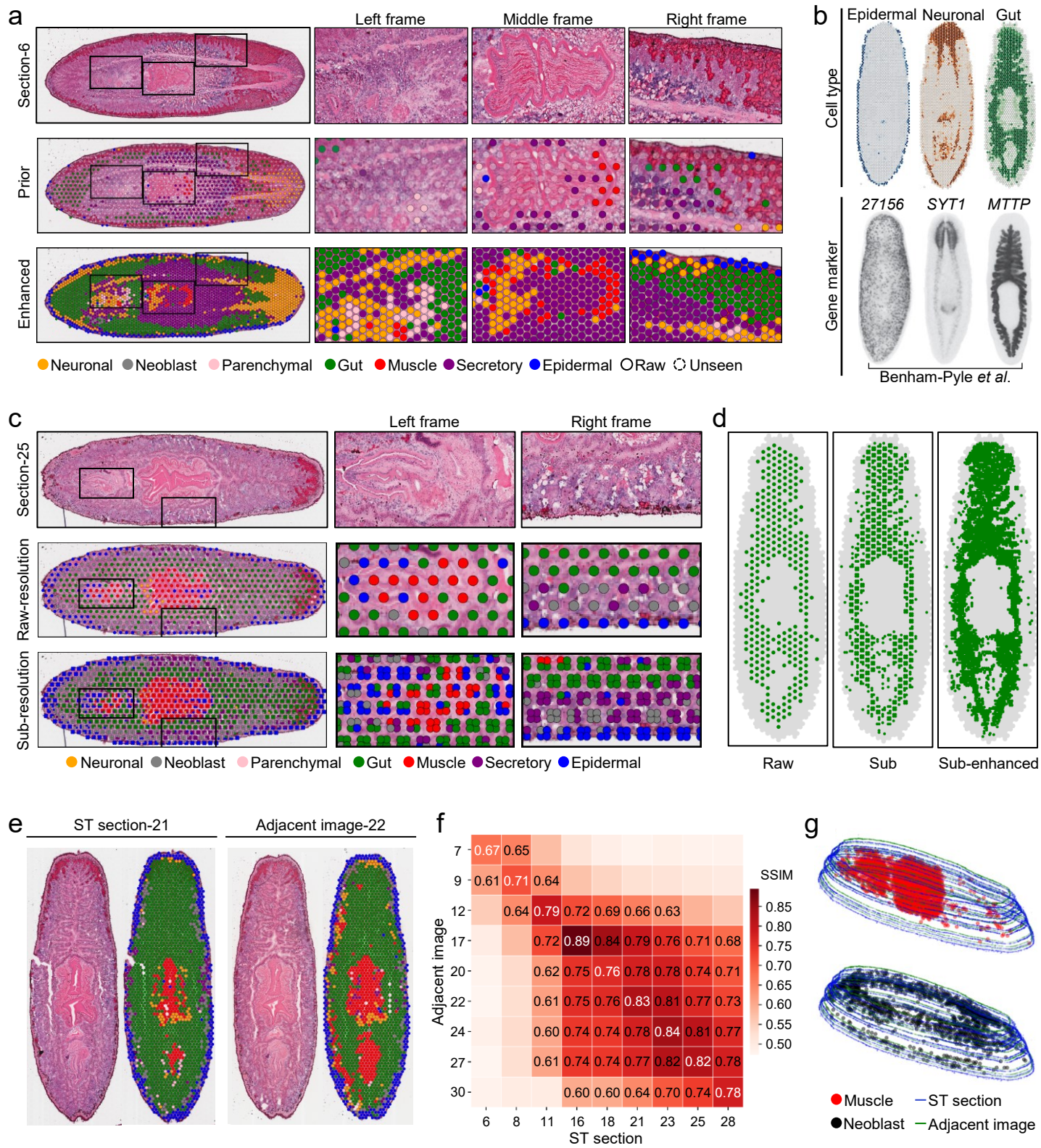
a
Left frame
Middle frame
Right frame
Section-6
Prior
Enhanced
Neuronal Neoblast Parenchymal Gut Muscle Secretory Epidermal Raw Unseen
b
Epidermal Neuronal Gut
Cell type
27156 SYT1 MTTP
Gene marker
Benham-Pyle et al.
c
Left frame
Right frame
Section-25
Raw-resolution
Sub-resolution
Neuronal Neoblast Parenchymal Gut Muscle Secretory Epidermal
d
Raw
Sub
Sub-enhanced
e
ST section-21
Adjacent image-22
f
SSIM
Adjacent image
ST section
g
Muscle
Neoblast
ST section
Adjacent image

Figure 4

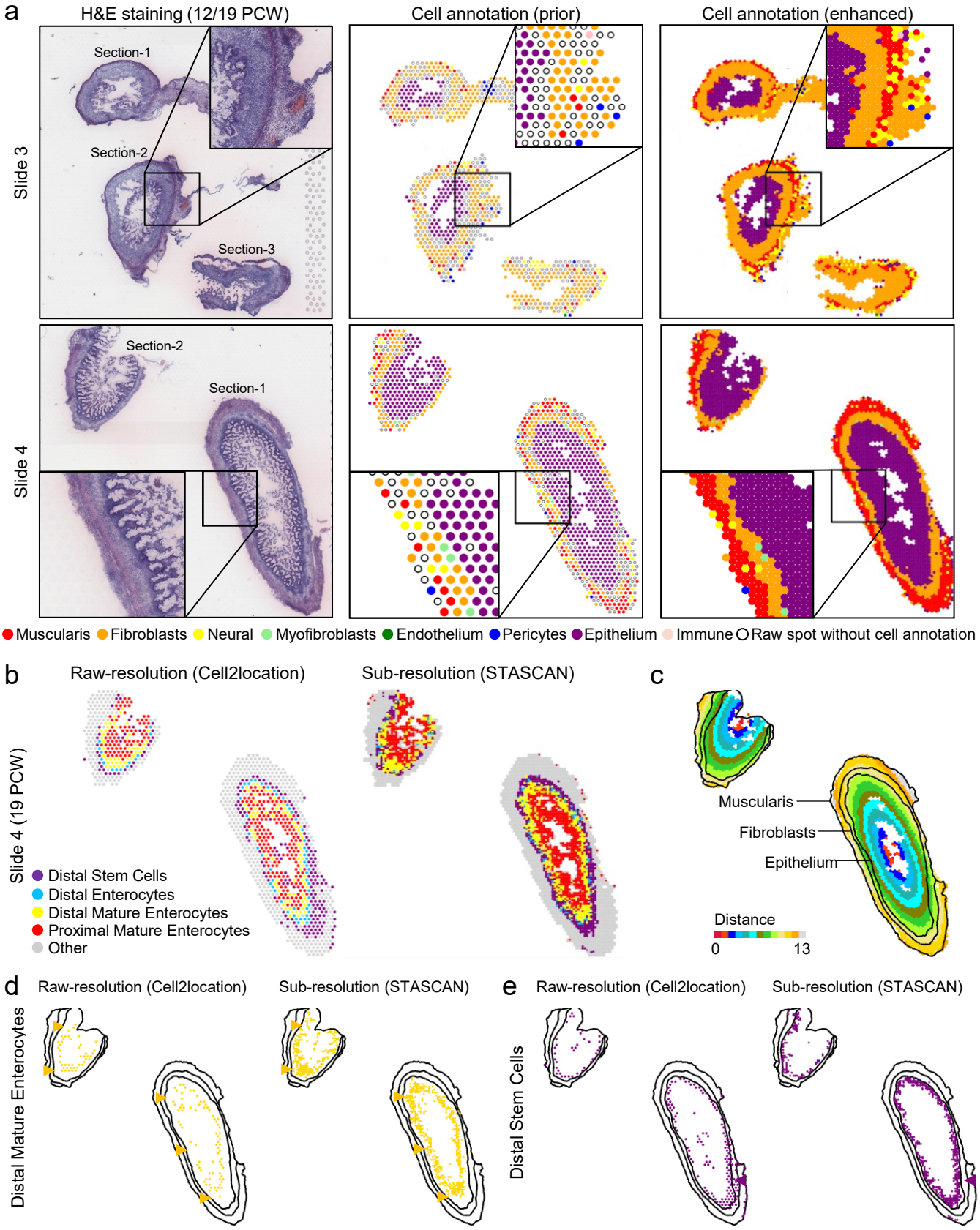
a
H&E staining (12/19 PCW)
Cell annotation (prior)
Cell annotation (enhanced)
Slide 3
Section-1
Section-2
Section-3
Slide 4
Section-2
Section-1
Muscularis
Fibroblasts
Neural
Myofibroblasts
Endothelium
Pericytes
Epithelium
Immune
Raw spot without cell annotation
b
Raw-resolution (Cell2location)
Sub-resolution (STASCAN)
Slide 4 (19 PCW)
Distal Stem Cells
Distal Enterocytes
Distal Mature Enterocytes
Proximal Mature Enterocytes
Other
c
Muscularis
Fibroblasts
Epithelium
Distance
0
13
d
Raw-resolution (Cell2location)
Sub-resolution (STASCAN)
Distal Mature Enterocytes
e
Raw-resolution (Cell2location)
Sub-resolution (STASCAN)
Distal Stem Cells

Figure 5

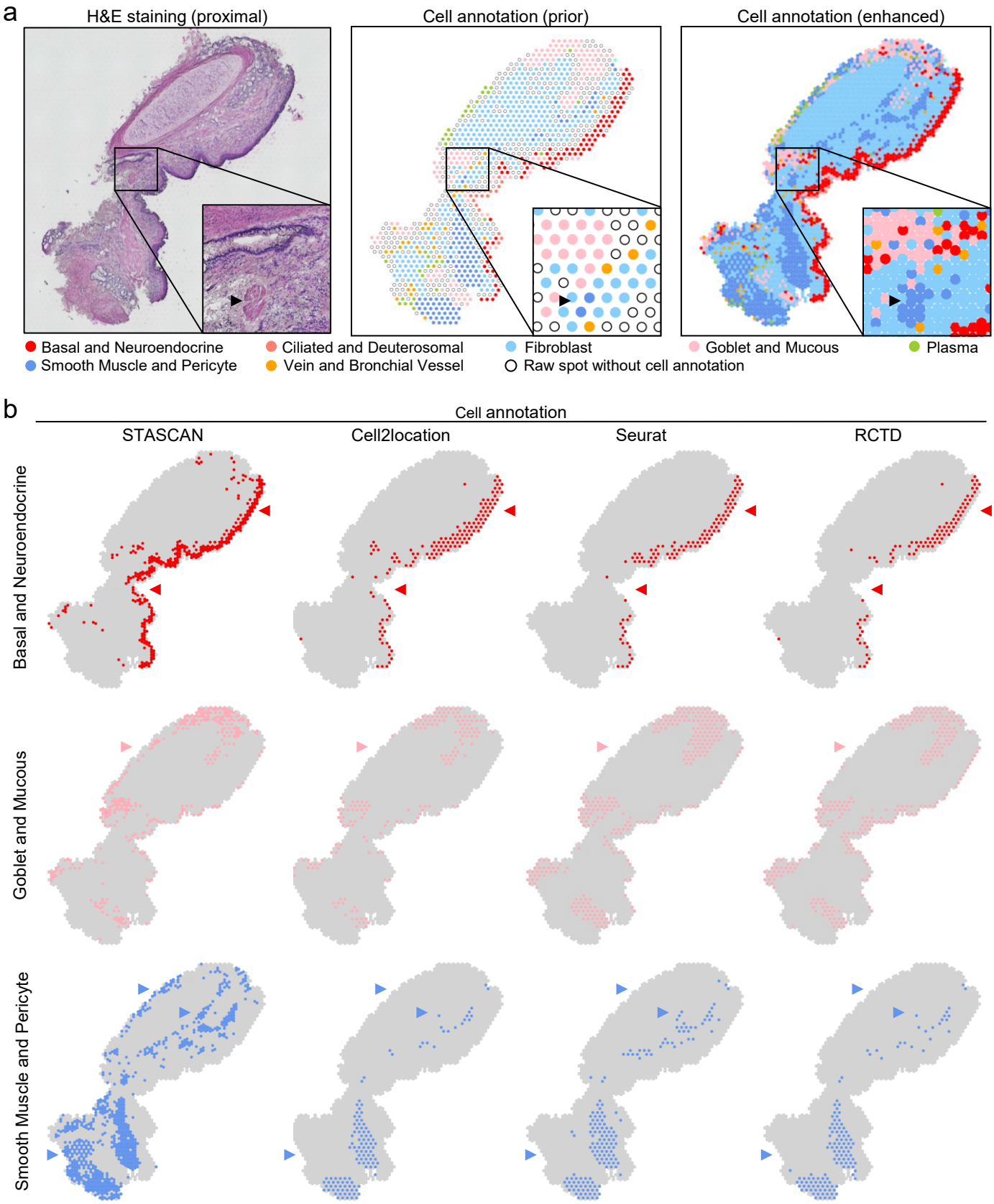
a
H&E staining (proximal)
Cell annotation (prior)
Cell annotation (enhanced)
Basal and Neuroendocrine
Ciliated and Deuterosomal
Fibroblast
Goblet and Mucous
Plasma
Smooth Muscle and Pericyte
Vein and Bronchial Vessel
Raw spot without cell annotation
b
Cell annotation
STASCAN
Cell2location
Seurat
RCTD
Basal and Neuroendocrine
Goblet and Mucous
Smooth Muscle and Pericyte

Figure 6

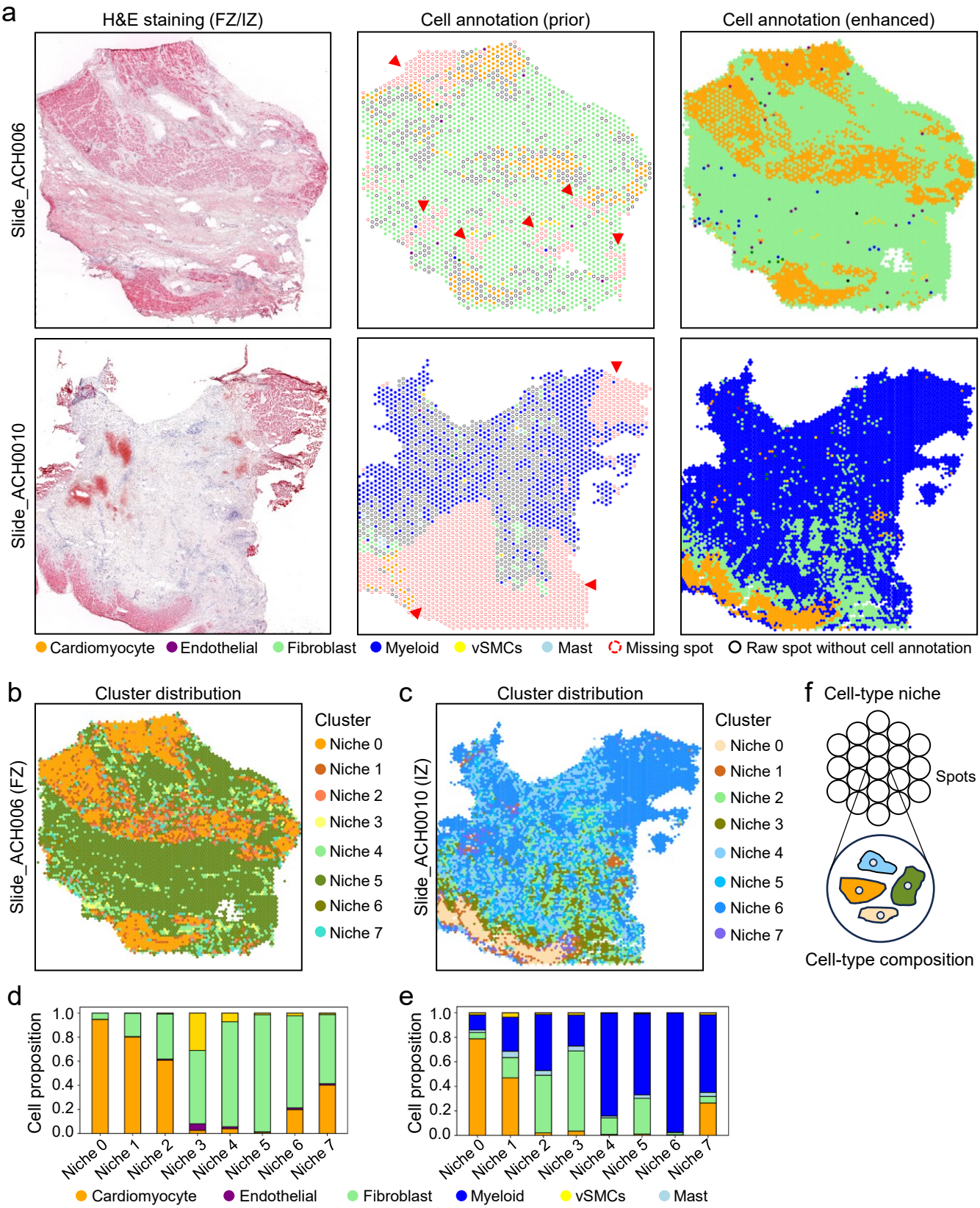
a
H&E staining (FZ/IZ)
Cell annotation (prior)
Cell annotation (enhanced)
Slide_ACH006
Slide_ACH0010
Cardiomyocyte
Endothelial
Fibroblast
Myeloid
vSMCs
Mast
Missing spot
Raw spot without cell annotation
b
Cluster distribution
Slide_ACH006 (FZ)
Cluster
Niche 0
Niche 1
Niche 2
Niche 3
Niche 4
Niche 5
Niche 6
Niche 7
c
Cluster distribution
Slide_ACH0010 (IZ)
Cluster
Niche 0
Niche 1
Niche 2
Niche 3
Niche 4
Niche 5
Niche 6
Niche 7
f
Cell-type niche
Spots
Cell-type composition
d
Cell proposition
1.0
0.8
0.6
0.4
0.2
0.0
Niche 0
Niche 1
Niche 2
Niche 3
Niche 4
Niche 5
Niche 6
Niche 7
e
Cell proposition
1.0
0.8
0.6
0.4
0.2
0.0
Niche 0
Niche 1
Niche 2
Niche 3
Niche 4
Niche 5
Niche 6
Niche 7
Cardiomyocyte
Endothelial
Fibroblast
Myeloid
vSMCs
Mast